Geophysical Prospecting

EAGE EUROPEAN ASSOCIATION OF GEOSCIENTISTS & ENGINEERS

*Geophysical Prospecting*, 2011, **59**, 635–650 doi: 10.1111/j.1365-2478.2011.00954.x

# Wave-equation migration velocity analysis with time-shift imaging

Tongning Yang* and Paul Sava

*Center for Wave Phenomena, Department of Geophysics, Colorado School of Mines, 1500 Illnois Str., Golden, CO 80401, USA*

Received September 2010, accepted January 2011

## ABSTRACT

Wave-equation migration velocity analysis is a technique designed to extract and update velocity information from migrated images. The velocity model is updated through the process of optimizing the coherence of images migrated with the known background velocity model. The capacity for handling multi-pathing of the technique makes it appropriate in complex subsurface regions characterized by strong velocity variation. Wave-equation migration velocity analysis operates by establishing a linear relation between a slowness perturbation and a corresponding image perturbation. The linear relationship and the corresponding linearized operator are derived from conventional extrapolation operators and the linearized operator inherits the main properties of frequency-domain wavefield extrapolation. A key step in the implementation is to design an appropriate procedure for constructing an image perturbation relative to a reference image that represents the difference between the current image and a true, or more correct image of the subsurface geology. The target of the inversion is to minimize such an image perturbation by optimizing the velocity model. Using time-shift common-image gathers, one can characterize the imperfections of migrated images by defining the focusing error as the shift of the focus of reflections along the time-shift axis. The focusing error is then transformed into an image perturbation by focusing analysis under the linear approximation. As the focusing error is caused by the incorrect velocity model, the resulting image perturbation can be considered as a mapping of the velocity model error in the image space. Such an approach for constructing the image perturbation is computationally efficient and simple to implement. The technique also provides a new alternative for using focusing information in wavefield-based velocity model building. Synthetic examples demonstrate the successful application of our method to a layered model and a subsalt velocity update problem.

**Key words:** Focusing error, Migration velocity analysis, Time-shift imaging.

## INTRODUCTION

In regions characterized by complex subsurface structure, prestack wave-equation depth migration, i.e. one-way wave-equation migration or reverse-time migration, is a powerful tool for accurately imaging the Earth's interior (Gray *et al.* 2001; Etgen, Gray and Zhang 2009). However, the quality of the final image greatly depends on the accuracy of the velocity model. Thus, a key challenge for seismic imaging in complex geology is an accurate determination of the velocity model in the area under investigation (Symes 2008; Woodward *et al.* 2008; Virieux and Operto 2009).

Migration velocity analysis (MVA) generally refers to tomographic methods implemented in the image domain. These velocity analysis techniques are based on the principle that the quality of the seismic image is optimized when the data are migrated with the correct velocity model. The techniques update

*E-mail: tyang@mines.edu

© 2011 European Association of Geoscientists & Engineers

the velocity model by optimizing the properties measuring the coherence of migrated images. As a result, the quality of both the image and velocity model is improved through the process of velocity analysis.

Typically, the input for MVA is represented by various types of common-image gathers, e.g., shot-domain (Al-Yahya 1989), surface-offset (Mulder and ten Kroode 2002), subsurface-offset (Rickett and Sava 2002), time-shift (Sava and Fomel 2006), angle-domain (Sava and Fomel 2003; Biondi and Symes 2004), or space- and time-lag extended-image gathers (Yang and Sava 2010; Sava and Vasconcelos 2011). Different kinds of image gathers determine whether semblance or focusing analysis should be used to measure the coherence of the image.

In practice, there are many possible approaches for implementing velocity analysis with different image gathers. However, all such realizations share a common element that they need a carrier of information to connect the input image gathers to the output velocity model. Thus, one can categorize velocity analysis techniques into ray-based and wavefield-based methods in terms of the information carrier they use. Ray-based methods, which are often described as traveltime velocity analysis, refer to techniques using wide-band rays as the information carrier (Bishop *et al.* 1985; Al-Yahya 1989; Stork and Clayton 1991; Woodward 1992; Stork 1992; Liu and Bleistein 1995; Jiao *et al.* 2002). Wavefield-based velocity analysis methods refer to techniques using band-limited wavefields as the information carrier (Biondi and Sava 1999; Mulder and ten Kroode 2002; Shen and Calandra 2005; Soubaras and Gratacos 2007; Xie and Yang 2008). Generally speaking, ray-based methods have advantages over wavefield-based methods in that they involve simple implementation and efficient computation. In contrast, wavefield-based methods are capable of handling complicated wave propagation phenomena that always occur in complex subsurface regions. Therefore, they are more robust and consistent with the wavefield-based migration techniques used in such regions. Furthermore, the resolution of wavefield-based methods is higher than that of ray-based methods because wavefield-based methods employ fewer approximations to wave propagation.

Different from traveltime velocity analysis methods, wavefield-based velocity analysis techniques require an image residual as the input, which is equivalent to the data misfit defined in the image domain. Wave-equation MVA (Sava and Biondi 2004a,b) and differential semblance optimization (Shen, Stolk and Symes 2003; Shen and Symes 2008) are two common wavefield-based velocity analysis approaches . The image residual for wave-equation MVA and differential semblance optimization are obtained either by constructing a linearized image perturbation (Sava, Biondi and Etgen 2005) or by applying a penalty operator to the offset- or angle-domain common-image gathers (Symes and Carazzone 1991; Shen and Calandra 2005), respectively.

Focusing analysis is a commonly used method for refining the velocity model (Faye and Jeannot 1986). It evaluates the coherence of migrated images by measuring the focusing of reflections in the image. The focusing information can be extracted from time-shift common-image gathers (Sava and Fomel 2006) and is quantified as the shift of the focus of reflections along the time-shift axis from the origin. Such a shift is often defined as a focusing error and indicates the existence of the velocity model error (MacKay and Abma 1992; Nemeth 1995). Therefore, the focusing error can be used for velocity model optimization. Wang *et al.* (2005) proposed a tomographic approach using focusing analysis for re-datuming data sets. The approach is a ray-based method and thus may become unstable when the multi-pathing problem exists due to complex geology. Higginbotham and Brown (2008) and Brown, Higginbotham and Clapp (2008) also propose a method to convert this focusing error into velocity updates using an analytic formula. This approach is based on 1D assumptions and the measured focusing error is transformed into vertical updates only. Hence, the method becomes less accurate in models with complex subsurface environments. Nevertheless, Wang *et al.* (2008, 2009) illustrated that focusing analysis can effectively improve the image quality and be used for updating the velocity model in subsalt areas.

For the implementation of wave-equation MVA, one important component is the construction of an image perturbation that is linked directly to a velocity perturbation. To construct the image perturbation, one first needs to measure the coherence of the image. Sava and Biondi (2004b) discussed two types of measurement for the imperfections of migrated images, i.e., focusing analysis (MacKay and Abma 1992; Lafond and Levander 1993) and moveout analysis (Yilmaz and Chambers 1984; Biondi and Sava 1999). The most common approach for constructing the image perturbation is to compare a reference image with its improved version. However, such an image-comparison approach has at least two drawbacks. First, the improved version of the image is always obtained by re-migration with one or more models, which is often computationally expensive. Second, if the reference image is incorrectly constructed, the difference between two images might exceed the small perturbation assumption. This can lead to cycle skipping that changes the convergence properties

of the inversion. An alternative to this approach, discussed in Sava and Biondi (2004a), uses prestack Stolt residual migration (Stolt 1996; Sava 2003) to construct a linearized image perturbation. This alternative approach avoids the cycle skipping problem but suffers from the approximation embedded in the underlying Stolt migration.

In this paper, we propose a new methodology for wavefield-based velocity analysis using focusing information of migrated images. The essential idea is to construct a linearized image perturbation from a time-shift imaging condition through focusing analysis and then use it for velocity updates. We demonstrate that such an image perturbation can be easily computed by a simple multiplication of the image derivative constructed from a background image and the measured focusing error. We also demonstrate that this type of image perturbation is fully consistent with the linearization embedded in wave-equation MVA. Finally, we illustrate the feasibility of our approach by testing the method on simple and complex synthetic data sets.

## THEORY

Under the single scattering approximation, seismic migration consists of two steps: wavefield reconstruction followed by the application of an imaging condition. We commonly consider a 'source' wavefield, originating at the seismic source and propagating in the medium prior to any interaction with the reflectors, and a 'receiver' wavefield, originating at discontinuities and propagating in the medium to the receivers (Berkhout 1982; Claerbout 1985). The two wavefields are kinematically equivalent at discontinuities of material properties. Any mismatch between the wavefields indicates inaccurate wavefield reconstruction typically assumed to be due to inaccurate velocity models. The source and receiver wavefields $u_s$ and $u_r$ are four-dimensional objects as functions of position $\mathbf{x} = (x, y, z)$ and frequency $\omega$,

$$u_s = u_s(\mathbf{x}, \omega), \tag{1}$$

$$u_r = u_r(\mathbf{x}, \omega). \tag{2}$$

An imaging condition is designed to extract from these extrapolated wavefields the locations where reflections occur in the subsurface. A conventional imaging condition (Claerbout 1985) forms an image as the zero cross-correlation lag between the source and receiver wavefields:

$$r(\mathbf{x}) = \sum_{\omega} \overline{u_s(\mathbf{x}, \omega)} u_r(\mathbf{x}, \omega), \tag{3}$$

where $r$ is the image of the subsurface and the overline represents a complex conjugation. An extended imaging condition (Sava and Fomel 2006) extracts the image by cross-correlation between the wavefields shifted by the time-lag $\tau$:

$$r(\mathbf{x}, \tau) = \sum_{\omega} \overline{u_s(\mathbf{x}, \omega)} u_r(\mathbf{x}, \omega) e^{2i\omega\tau}. \tag{4}$$

Other possible extended imaging conditions include space-lag extension (Rickett and Sava 2002) or space- and time-lag extensions (Sava and Vasconcelos 2011) but we do not discuss these types of imaging conditions here.

In the process of seismic migration, if the source and receiver wavefields are extrapolated with the correct velocity model, the result of cross-correlation between reconstructed wavefields, i.e., the migrated image, is maximized at zero lags. In other words, if the velocity used for migration is correct, reflections in the image are focused at zero offset and zero time. If the source and receiver wavefields are extrapolated with an incorrect velocity model, the result of cross-correlation is not maximized at zero lags. As a consequence, reflections in the image are focused at non-zero time but zero offset. This indicates the existence of error for downward continuation of the reconstructed wavefields. In such a situation, we can apply focusing analysis and extract the information about the accuracy of the velocity model. A commonly used approach for focusing analysis is to measure the focusing error in either the depth domain or time domain. The depth-domain focusing error is defined as the depth difference between focusing depth $d_f$ and migration depth $d_m$ (MacKay and Abma 1992)

$$\Delta z = d_f - d_m, \tag{5}$$

where

$$d_f = \frac{d}{\rho}, \tag{6}$$

and

$$d_m = d\rho. \tag{7}$$

Here $d$ is the true depth of the reflection point, $\rho = \frac{V_m}{V}$ is the ratio between migration and true velocities. The time-domain focusing error is defined as the time-shift being applied to the reconstructed wavefields to achieve focusing of reflections. Yang and Sava (2010) quantitatively analyzed the influence of the velocity model error on the focusing property of reflections and derived the formula connecting the depth-domain and time-domain focusing error:

$$\Delta\tau = \frac{d_f - d_m}{V_m}, \tag{8}$$

where $V_m$ represents the migration velocity. Notice that the formulae for $d_f$ and $d_m$ are derived under the assumptions of constant velocity, small offset angle and horizontal reflector. As a consequence, the analytic formula in equation (8) is an approximation of the true focusing error, and has limited applicability in practice.

To use wave-equation MVA for model building, one needs to start from linearization of the problem since an image is usually a non-linear function of the velocity model. Furthermore, a non-linear optimization problem is more difficult to solve than a linear optimization problem. We represent the true slowness as the sum of background slowness $s_b$ and slowness perturbation $\Delta s$:

$$s(\mathbf{x}) = s_b(\mathbf{x}) + \Delta s(\mathbf{x}). \tag{9}$$

Likewise, the image can also be characterized as a sum of background image $r_b$ and image perturbation $\Delta r$:

$$r(\mathbf{x}) = r_b(\mathbf{x}) + \Delta r(\mathbf{x}). \tag{10}$$

The perturbations $\Delta s$ and $\Delta r$ are related by the wave-equation tomographic operator $\mathbf{L}$ derived from the linearization of the one-way wave-equation migration operator, as demonstrated by Sava and Biondi (2004a). A brief summary of derivation and construction of $\mathbf{L}$ can be found in Appendix A. Consequently, we can establish a linear relationship between the image and slowness perturbations:

$$\Delta r = \mathbf{L}\Delta s. \tag{11}$$

Sava and Vlad (2008) further illustrated the implementation of operator $\mathbf{L}$ for different imaging configurations, i.e., zero-offset, survey-sinking and shot-record cases.

The information of focusing error $\Delta\tau$ is available on the extended images constructed with equation (4). In other words, the focus of reflections can be evaluated by locating the maximum energy of reflection events in time-shift common-image gathers. If the focus is located at zero time shift, the velocity model is correct. Otherwise, the distance of the focus from the origin is measured along the time-shift axis and defined as the focusing error. Then, an improved image $\widetilde{r}$ can be obtained by choosing the image from the time-shift common-image gather at the $\tau$ value corresponding to the focusing error:

$$\widetilde{r}\,(\mathbf{x}) = r\,(\mathbf{x}, \tau)|_{\tau=\Delta\tau}\,, \tag{12}$$

and an image perturbation can be constructed by direct subtraction:

$$\Delta r\,(\mathbf{x}) = \widetilde{r}\,(\mathbf{x}) - r_b(\mathbf{x}). \tag{13}$$

Although such an approach is straightforward, the constructed image perturbation might be phase-shifted too much with respect to background image $r_b$ and thus violates the Born approximation required by tomographic operator $\mathbf{L}$. To overcome the challenge, Sava and Biondi (2004a) proposed to construct a linearized image perturbation as

$$\Delta r\,(\mathbf{x}) \approx \mathbf{K}'\big|_{\rho=1}\,[r_b]\Delta\rho, \tag{14}$$

where $\mathbf{K}$ is the prestack Stolt residual migration operator (Stolt 1996; Sava 2003), the $'$ sign represents derivation relative to the velocity ratio $\rho$ and $\Delta\rho = \rho - 1$. Similarly, we can also construct an image perturbation by the linearization of the image relative to the time-shift parameter $\tau$:

$$\Delta r\,(\mathbf{x}) \approx \left.\frac{\partial r\,(\mathbf{x}, \tau)}{\partial \tau}\right|_{\tau=0} \Delta\tau, \tag{15}$$

where the image derivative with respect to time-shift $\tau$ is

$$\frac{\partial r\,(\mathbf{x}, \tau)}{\partial \tau} = \sum_{\omega} (2i\omega)\,\overline{u_s\,(\mathbf{x}, \omega)}u_r\,(\mathbf{x}, \omega)\,e^{2i\omega\tau}. \tag{16}$$

By constructing the image perturbation with equation (15), one can avoid the cycle-skipping problem because the linearized image perturbation is obtained from the background image and thus has no phase shift with respect to the background image. Furthermore, equation (15) provides a straightforward way to convert the focusing error associated with the velocity model error into the image perturbation. In other words, equation (15) maps the velocity error into the image domain, so that one can optimize the model by minimizing the image perturbation. The linearization of both the approaches in equations (14) and (15) is consistent with the characteristics of tomographic operator $\mathbf{L}$.

One can follow the procedure outlined below to construct the image perturbations from time-shift imaging condition and use it for wavefield-based velocity optimization:

- Migrate the data and output time-shift common-image gathers according to equation (4);
- Measure $\Delta\tau$ on time-shift common-image gather panels by picking the focus, i.e., maximum energy, for all reflections;
- Construct the image derivative according to equation (16);
- Construct the linearized image perturbation according to equation (15).

After we construct image perturbation $\Delta r$, we can solve for slowness perturbation $\Delta s$ by minimizing the objective function,

$$J\,(\Delta s) = \frac{1}{2}\|\Delta r - \mathbf{L}\Delta s\|^2. \tag{17}$$

Such an optimization problem can be solved iteratively using conjugate-gradient-based methods. As most practical inverse problems are ill-posed, additional constraints must be imposed during the inversion to obtain a stable and convergent result. This can be done by adding a model regularization term in the objective function equation (17), leading to the modified objective function:

$$J(\Delta s) = \frac{1}{2}\|\Delta r - \mathbf{L}\Delta s\|^2 + \alpha^2\|\mathbf{A}\Delta s\|^2, \tag{18}$$

where $\alpha$ is a scalar to control the relative weights between the data residual and model norm and $\mathbf{A}$ is a regularization operator (Fomel 2007). How to chose $\mathbf{A}$ and $\alpha$ is outside the scope of discussion in this paper.

## EXAMPLES

We illustrate our methodology with two synthetic examples. The first example consists of four dipping layers with different thickness and dipping angle. The velocities of the four layers are 1.5, 1.6, 1.7 and 1.8 km/s, respectively. The background model is constant with a velocity of 1.5 km/s. Figure 1(a,b) shows the true and background velocity models, respectively. Figure 2(a,b) are the image migrated with the true and background velocity model, respectively. Comparing these two images, one can observe that the second and third reflectors in Fig. 2(b) are positioned incorrectly due to the error of the velocity model.

Figure 3(a-c) shows three time-shift common-image gathers migrated with the background model. The image gathers are chosen at $x = 1.2$, $x = 1.8$ and $x = 2.3$ km, respectively. The

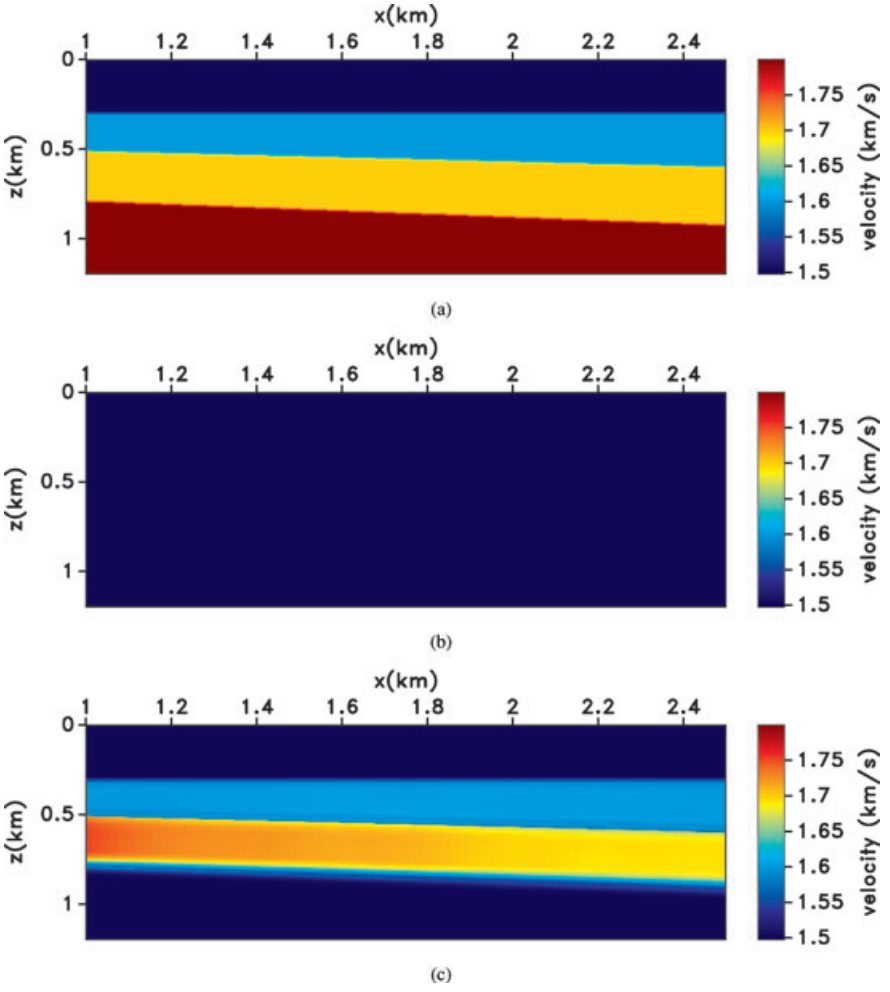



**Figure 1** Velocity profiles of the layers model. a) The true velocity model. b) The background velocity model with a constant velocity of the first layer 1.5 km/s. c) The updated velocity model.

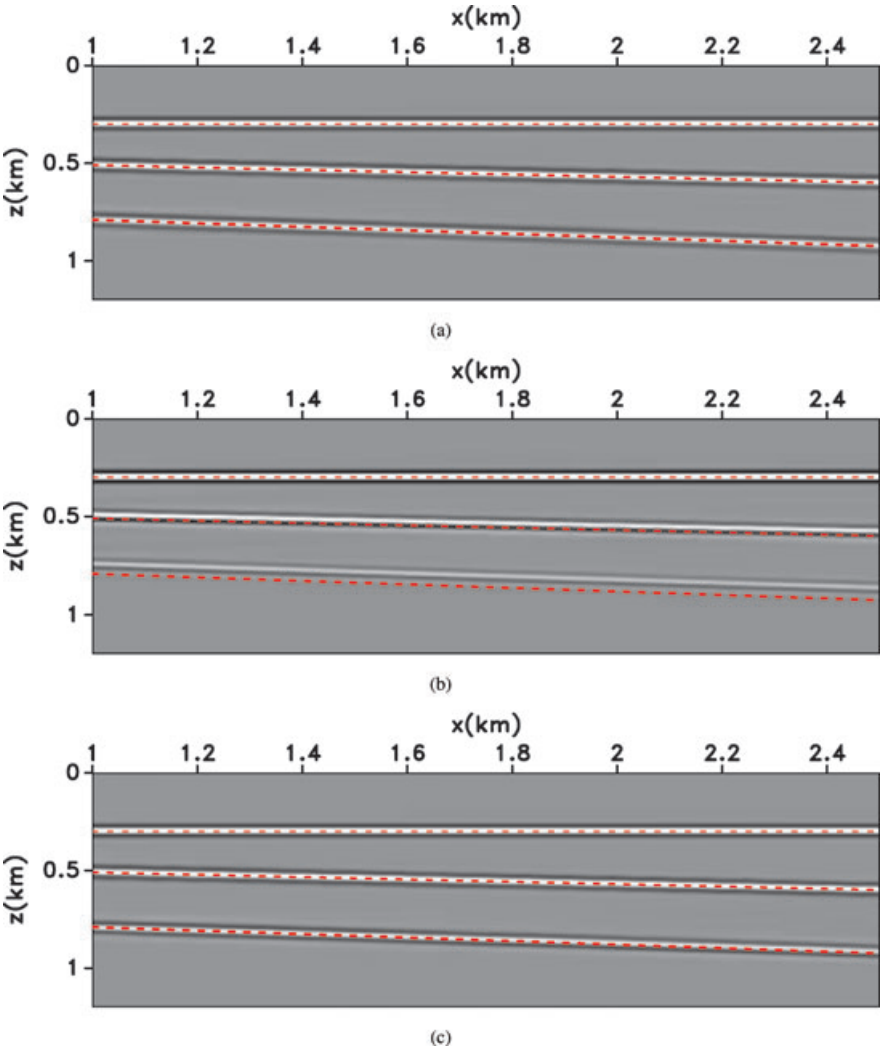



**Figure 2** Images migrated with a) the true velocity model, b) the background velocity model and c) the updated velocity model. The dash lines represent the true position of the reflections.

focusing error picking is done by applying an automatic picker to the envelope of the original image gathers. The solid lines in the figure plot the picked focusing error, while the dashed lines represent zero time shift. In this case, as the velocity errors for the second and third layers increase with depth, the focusing error increases with depth accordingly. As a result, bigger time shifts can be observed for deeper events. Figure 4(a) shows the focusing error as a function of position and depth. This figure depicts the focusing error picked from the image gathers constructed at every horizontal location $x$. Since the layers have different thickness, the associated velocity errors change as a function of horizontal and vertical directions. Therefore, a spatially varying focusing error of the subsurface is observed.

We construct the image perturbation using the procedure discussed in the preceding sections. Next, we perform the inversion based on the objective function in equation (18). The inverse problem is solved using the conjugate-gradient method. For this simple model, two non-linear iterations are enough to reconstruct the velocity model.

Figure 1(c) shows the updated model after the inversion. The velocities for the second and third layers are correctly inverted. Here, the velocity update occurs in the region above the fourth layer. This is due to the fact that no reflection exists in the bottom part of the model and the input image perturbation carries no velocity information for the bottom layer. Thus, the inversion does not compute velocity updates in the area. Figure 2(c) shows the image migrated with the

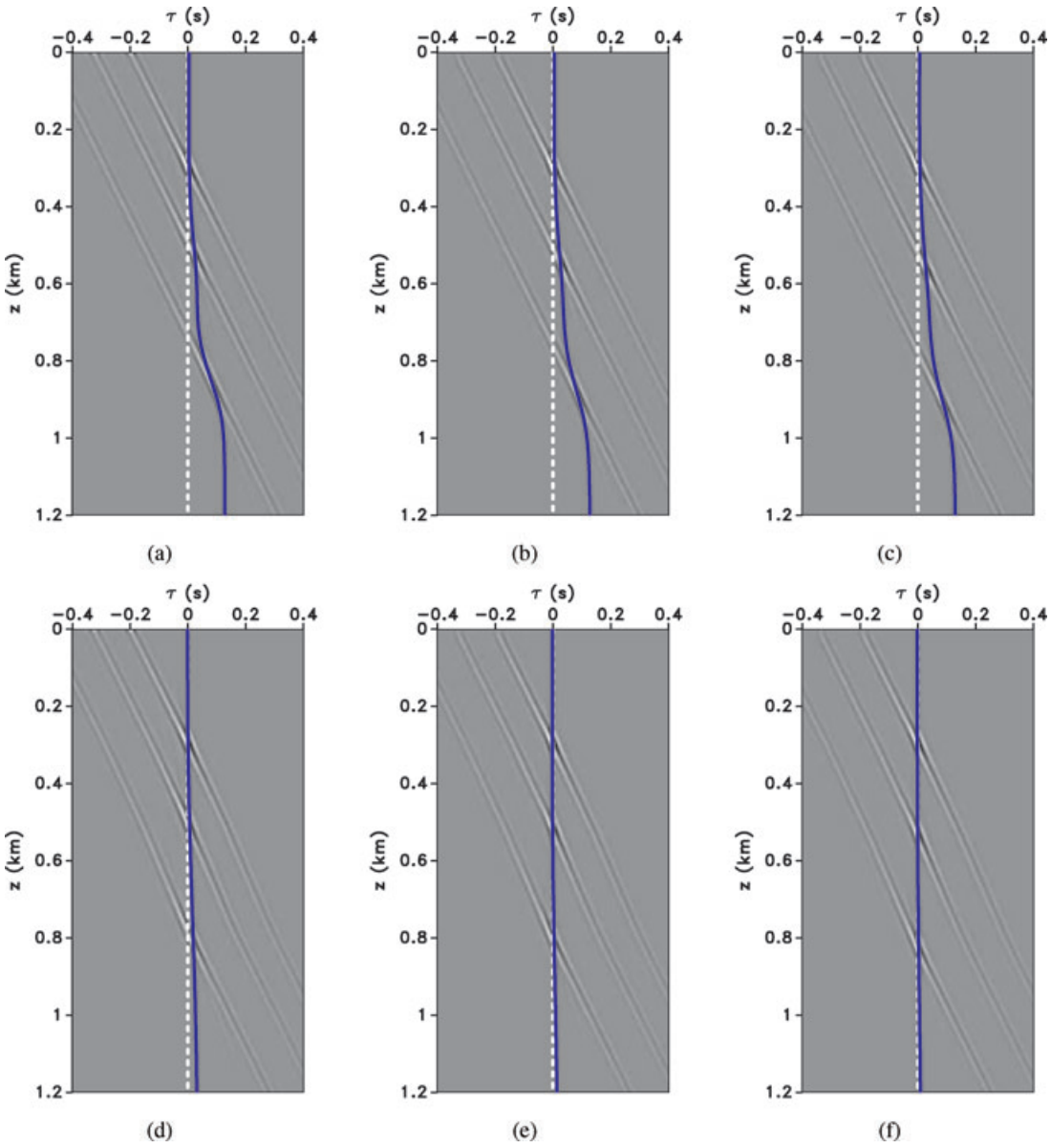



**Figure 3** Time-shift CIGs migrated with the background model a) at $x = 1.2$ km, b) at $x = 1.8$ km and c) at $x = 2.3$ km. Time-shift CIGs migrated with the updated model at d) $x = 1.2$ km, e) at $x = 1.8$ km and f) at $x = 2.3$ km. The overlain solid lines represent picked focusing error. The dash lines represent zero time shift.

updated model. The reflections are positioned in the correct depth, as compared with Fig. 2(a) and indicated by the dashed lines overlain on the figure.

Figure 3(d-f) shows image gathers obtained by migration with the updated model. The gathers are chosen at the same positions as the gathers shown in Fig. 3(a-c), i.e., at $x = 1.2$, $x = 1.8$ and $x = 2.3$ km, respectively. The focus of all the reflections is located at zero time-shift, as demonstrated by the fact that the solid and dashed lines are overlapped with each other in the gathers. Figure 4(b) is the focusing error panel of the subsurface. The value of the focusing error is zero almost everywhere. This means that the inversion has achieved the target of minimizing the focusing error and confirms the successful reconstruction of the velocity model in this example.

We also apply our methodology to a subsalt velocity update example. The target area is chosen from the subsalt portion of the Sigsbee 2A model (Paffenholz *et al.* 2002), ranging from

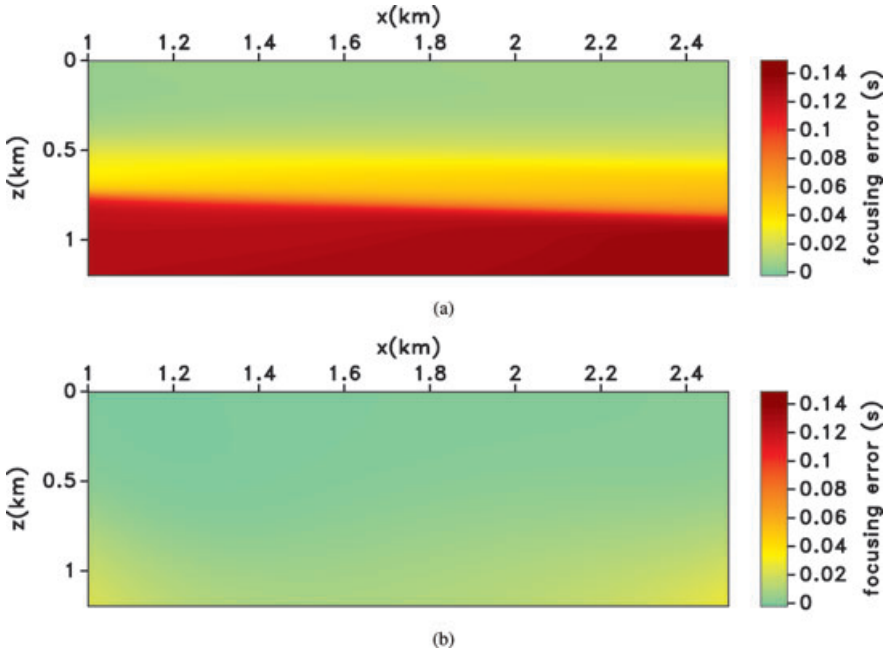



**Figure 4** a) Focusing error panel corresponding to the background model. b) Focusing error panel corresponding to the updated model.

$x = 9.5$ km, $z = 5.0$ km to $x = 18.5$ km, $z = 9.3$ km. For this example, the main goals are to image correctly the fault located between the point $x = 14.0$ km, $z = 6.0$ km and the point $x = 16.0$ km, $z = 9.0$ km, to increase the focusing for the deeper diffractors and to position correctly the bottom flat reflector. We assume correct knowledge of the velocity above the salt and known salt geometry. The background model for the target zone is obtained by scaling the true model with a constant factor 0.9. The true and background velocity models are depicted in Fig. 5(a,b), respectively. Figure 6(a,b) shows the images migrated with the true and background model, respectively. Due to the error of the background velocity model, the fault is obscured by nearby sediment reflections, the deeper diffractions are defocused and the bottom flat reflector is positioned far away from its correct depth.

Figure 7(a-c) shows several time-shift common-image gathers migrated with the background model at $x = 13.0$, $x = 14.8$ and $x = 16.6$ km, respectively. The picked focusing error is directly overlain on the gathers, although the picking is done on the envelope of the original image gathers just as the previous example. Here, we notice that the picks do not start at zero on the top of the gathers, although the associated focusing error should be zero. Such an error is mainly caused by the truncation of reflections in the gathers. Figure 8(a) shows the focusing error in the target area. Notice that variation exists for the picked focusing error in lateral and vertical directions. Part of such a variation is caused by the uneven illumination of the subsalt area, which may lead to difficulties for the automatic picker.

Next, we use the same procedure to construct the image perturbation as introduced in the preceding section. Then we run the inversion to obtain the velocity update by minimizing the objective function in equation (18). Figure 5(c) shows the updated model after three nonlinear iterations. The inversion has correctly reconstructed the velocity model in the subsalt area. Figure 6(c) shows the image migrated with the updated model. The fault located between the point $x = 14.0$ km, $z = 6.0$ km and the point $x = 16.0$ km, $z = 9.0$ km is delineated and clearly visible in the image. The bottom reflector is positioned at the correct depth and becomes more coherent. The deeper diffractions are also well focused. These improvements in the image imply a correct update of the velocity model.

Figure 7(d-f) plots several image gathers migrated with the background model at $x = 13.0$, $x = 14.8$ and $x = 16.6$ km, respectively. The focusing error picks are overlain on the gathers. Most reflections are focused at zero time shift, which means the focusing error is reduced thanks to the more accurate velocity model after the inversion. Figure 8(b) plots the focusing error in the target area after velocity update and remigration. The focusing error is reduced after the inversion, which indicates the successful optimization of the velocity model.

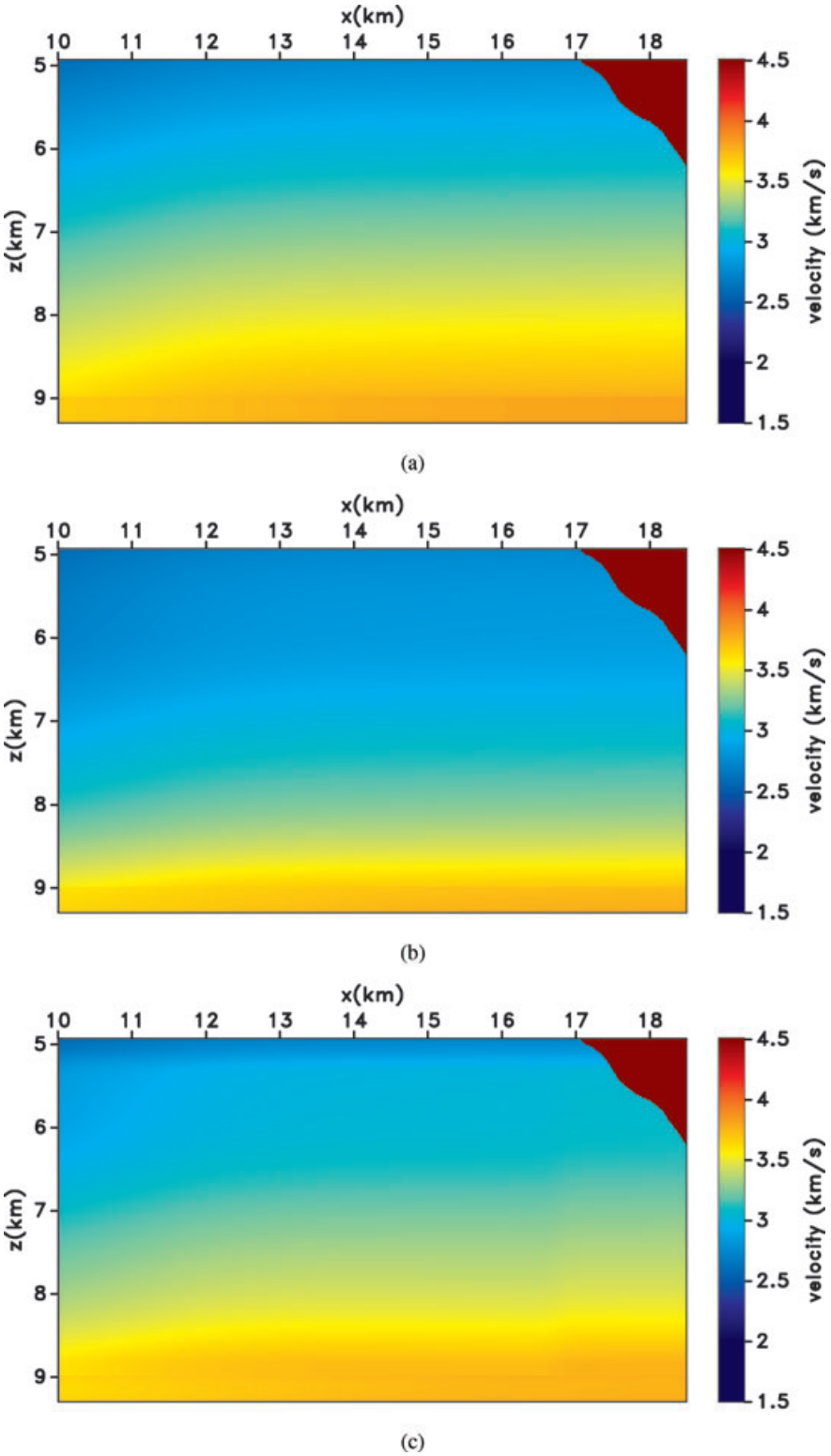



**Figure 5** Velocity profiles of Sigsbee 2A model. a) The true velocity model, b) the background velocity model and c) the updated model.

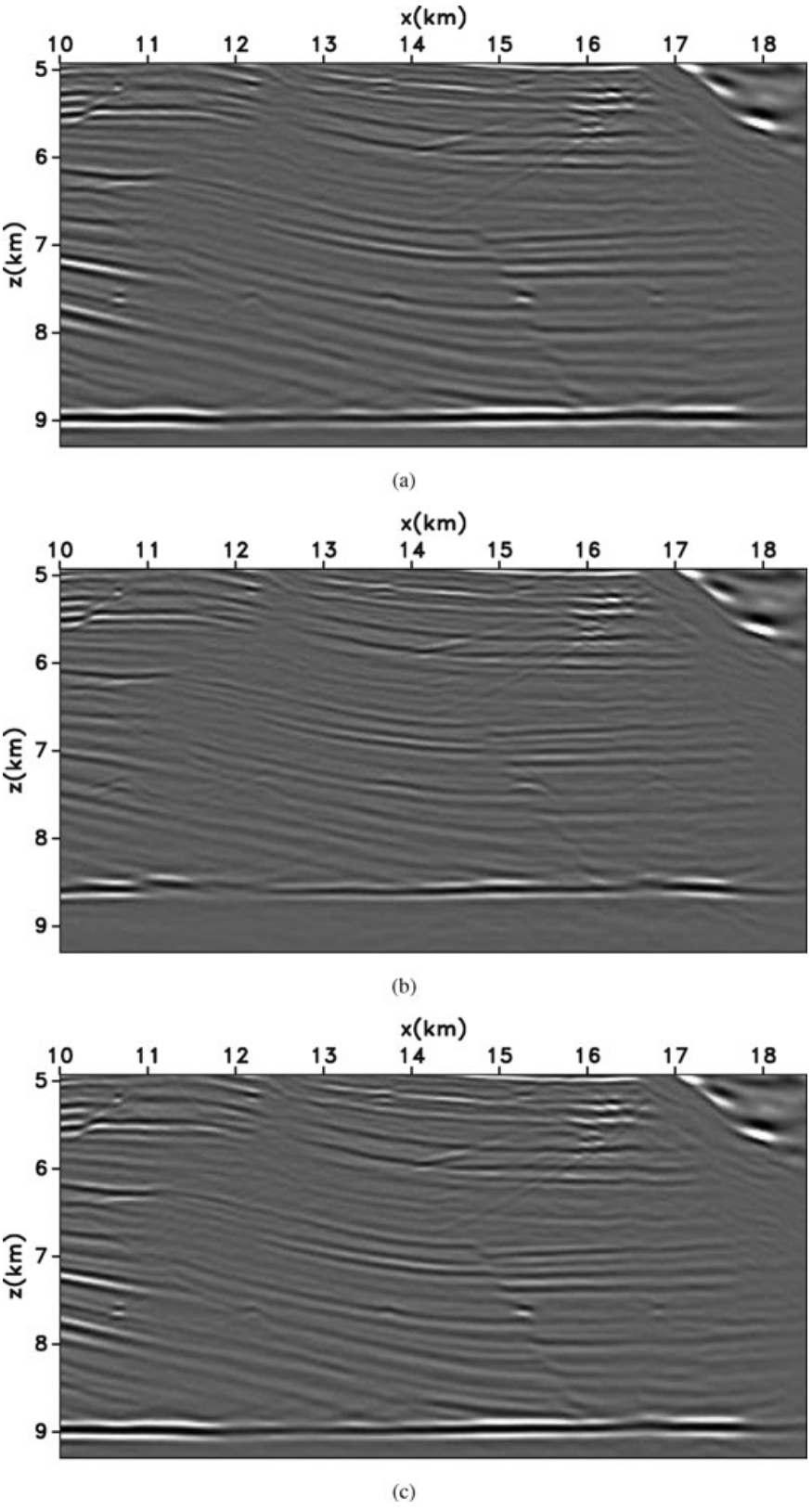



**Figure 6** Images migrated with a) the true velocity model, b) the background velocity model and c) the updated model.

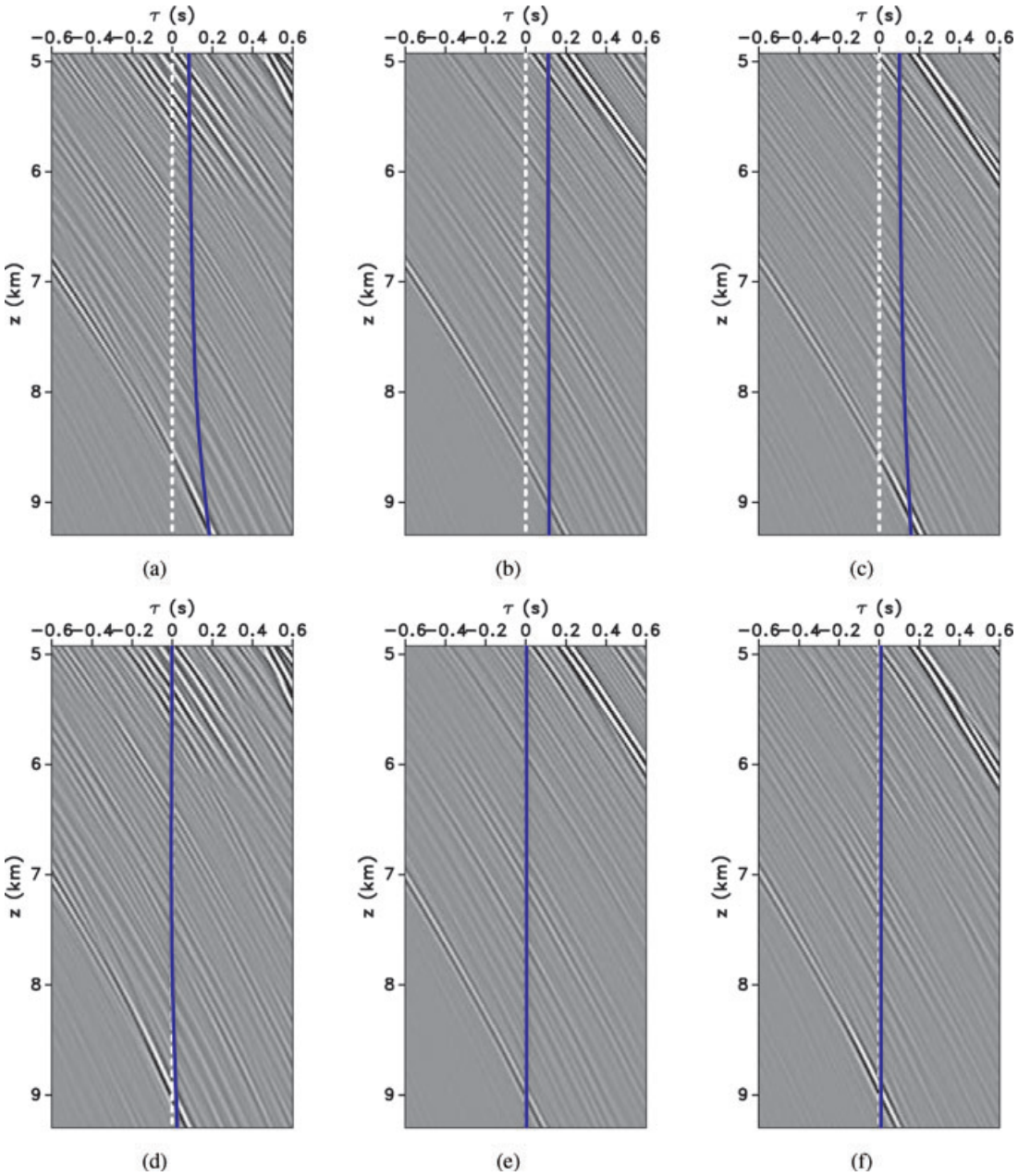



**Figure 7** Time-shift CIGs migrated with the background model a) at $x = 13.0$ km, b) at $x = 14.8$ km and c) at $x = 16.6$ km. Time-shift CIGs migrated with the updated model d) at $x = 13.0$ km, e) at $x = 14.8$ km and f) at $x = 16.6$ km. The overlain solid lines represent picked focusing error. The dash lines represent zero time shift.

To further confirm that the velocity model is correctly inverted, we also compute angle-domain common-image gathers with the background and updated models and use the flatness of reflection events in the gathers as the criterion to evaluate the result of the inversion. The angle-domain gahthers are chosen at the same locations as the time-shift gathers. Figure 9(a-c) plots the gathers corresponding to the background velocity model, while Fig. 9(d-f) shows the gathers for the updated velocity model. In comparison, the reflection events in the gathers obtained with the updated model are flatter than the events in the gathers obtained with the background model. This demonstrates the improvement of

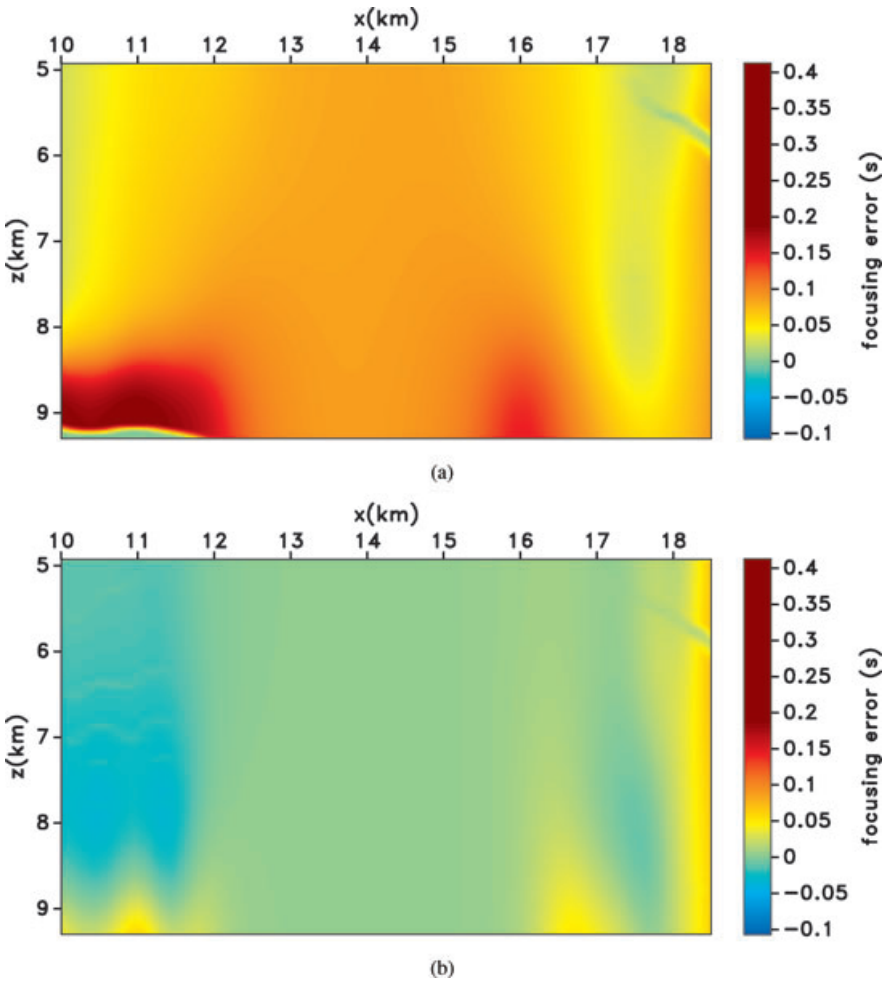



**Figure 8** a) Focusing error panel corresponding to the background model. b) Focusing error panel corresponding to the updated model.

the quality of the velocity model after the optimization. However, we notice that the curvature of the residual moveout in the gathers obtained with the background model is not easily distinguishable. This can cause difficulties for curvature picking and thus degrades the velocity estimation methods relying on flatting the residual moveout. In such a situation, minimizing the focusing error, as in the case of our approach, may provide a reliable alternative for velocity optimization.

## DISCUSSION

Using focusing information extracted from time-shift imaging offers a good alternative to wavefield-based velocity model optimization. The key to the approach is to construct a linearized image perturbation associated with the focusing error. The computation of the linearized image perturbation is simple and straightforward. Also, the cost of the construction is trivial as no expensive re-migration scan and angle decomposition are required in this procedure. Furthermore, such a velocity analysis method based on time-shift image gathers is computationally more attractive in 3D application as only one additional dimension is required for constructing image gathers, while two additional dimensions are needed for constructing lag-domain image gathers(Shen and Symes 2008).

The inversion scheme described in the paper is a wave-equation-based tomographic approach. Although the information is extracted by applying focusing analysis to time-shift image gathers, the process of velocity updating does not rely on any analytic formulae as in the case for conventional depth-focusing analysis. Therefore, the technique discussed in this paper has applicability to models with arbitrary lateral velocity variations.

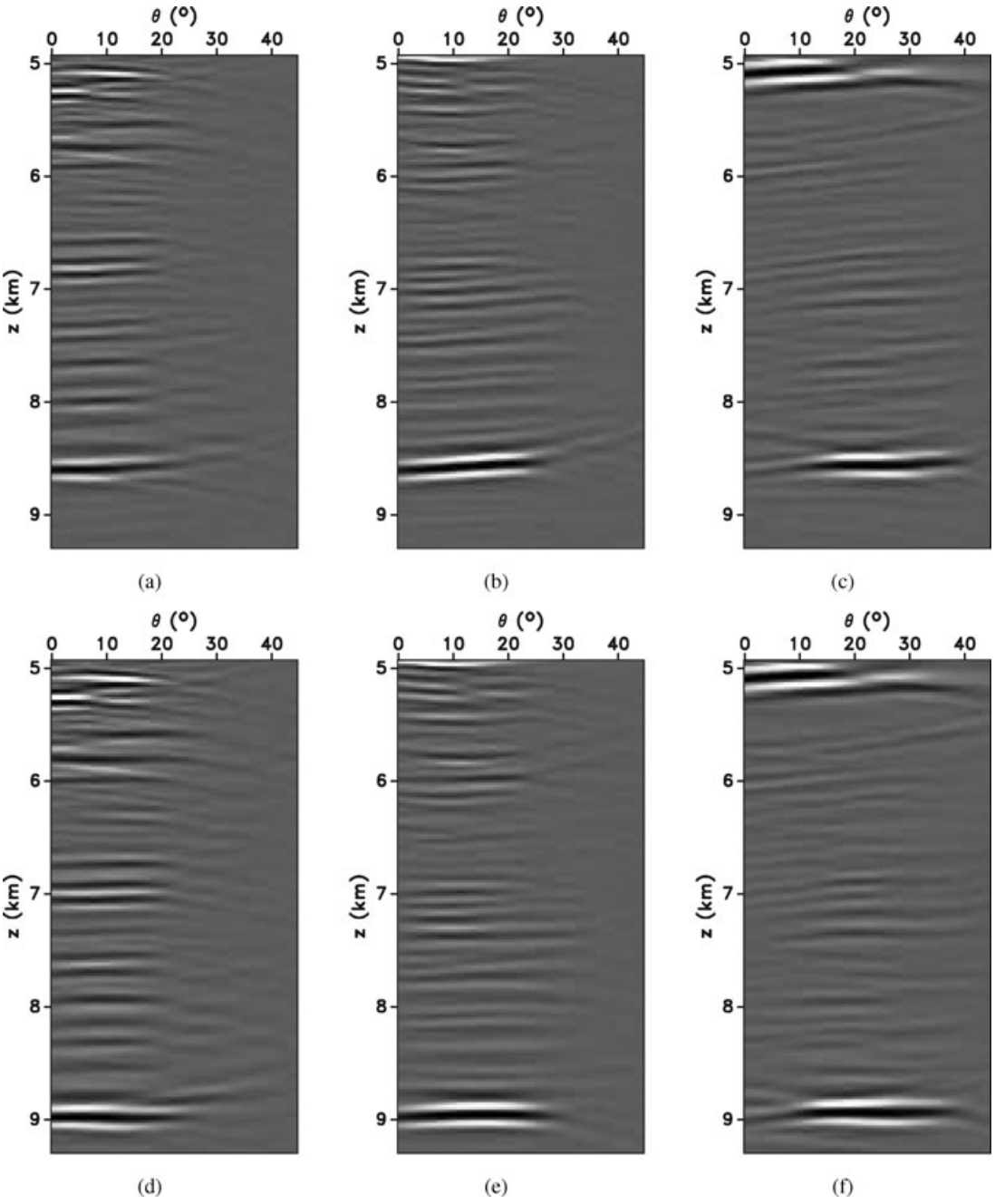



**Figure 9** Angle-domain CIGs migrated with the background model a) at $x = 13.0$ km, b) at $x = 14.8$ km and c) at $x = 16.6$ km. Angle-domain CIGs migrated with the updated model d) at $x = 13.0$ km, e) at $x = 14.8$ km and f) at $x = 16.6$ km.

Finally, we emphasize that picking the focusing error is extremely important for our approach as the focusing error determines the direction and magnitude of the velocity update. Therefore, the process of the picking should be carefully implemented.

## CONCLUSIONS

We develop a new method for implementing wave-equation migration velocity analysis based on time-shift imaging and focusing analysis. The objective of the velocity optimization

is to minimize the focusing error measured from time-shift image gathers. The methodology relies on constructing linearized image perturbations by applying focusing analysis to the image gathers. The focusing error is defined as the shift of the focus for reflections along the time-shift axis and provides a measurement for the accuracy of the velocity model used in migration. We use this information in conjunction with image derivatives relative to the time-shift parameter to compute linearized image perturbations as the input for velocity model optimization. The image perturbation obtained by this approach is consistent with the Born approximation used for the wave-equation tomographic operators so that the cycle-skipping problem can be avoided. The construction of the image perturbation in our approach is efficient, since the main cost is just the construction of the time-shift image gathers and is much lower than the cost of re-migration scans and angle decomposition. In addition, our method is accurate, since it does not include strong assumptions about the smoothness of the background model when constructing the linearized image perturbation. Thus, our approach is suitable for areas with complex subsurface structure. The synthetic examples demonstrate the validity of the linearized image perturbation constructed using our new method. The inversion with such an image perturbation as the input can render satisfactory updates for the velocity model. The success of the velocity optimization is confirmed by the fact that the focusing error is reduced after the inversion.

## ACKNOWLEDGEMENTS

We acknowledge the support of the sponsors of the Center for Wave Phenomena at Colorado School of Mines. This work is also partially supported by a research grant from Statoil. The reproducible numeric examples in this paper use the Madagascar open-source software package freely available from http://www.reproducibility.org.

## REFERENCES

Al-Yahya K.M. 1989. Velocity analysis by iterative profile migration. *Geophysics* **54**, 718–729.

Berkhout A.J. 1982. *Imaging of Acoustic Energy by Wave Field Extrapolation*. Elsevier.

Biondi B. and Sava P. 1999. Wave-equation migration velocity analysis. 69th SEG meeting, Houston, Texas, USA, Expanded Abstracts, 1723–1726.

Biondi B. and Symes W. 2004. Angle-domain common-image gathers for migration velocity analysis by wavefield-continuation imaging. *Geophysics* **69**, 1283–1298.

Bishop T.N., Bube K.P., Cutler R.T., Langan R.T., Love P.L., Resnick J.R., Shuey R.T., Spindler D.A. and Wyld H.W. 1985. Tomographic determination of velocity and depth in laterally varying media. *Geophysics* **50**, 903–923. (Slide set available from SEG Publications Department).

Brown M.P., Higginbotham J.H. and Clapp R.G. 2008. Velocity model building with wave equation migration velocity focusing analysis. 78th SEG meeting, Las Vegas, Nevada, USA, Expanded Abstracts, 3078–3082.

Claerbout J.F. 1985. *Imaging the Earth's Interior*. Blackwell Scientific Publications.

Etgen J., Gray S.H. and Zhang Y. 2009. An overview of depth imaging in exploration geophysics. *Geophysics* **74**, WCA5–WCA17.

Faye J.P. and Jeannot J.P. 1986. Prestack migration velocities from focusing depth analysis. 56th SEG meeting, Houston, Texas, USA, Expanded Abstracts, 438–440.

Fomel S. 2007. Shaping regularization in geophysical-estimation problems. *Geophysics* **72**, R29–R36.

Gray S.H., Etgen J., Dellinger J. and Whitmore D. 2001. Seismic migration problems and solutions. *Geophysics* **66**, 1622–1640.

Higginbotham J.H. and Brown M.P. 2008. Wave equation migration velocity focusing analysis. 78th SEG meeting, Las Vegas, Nevada, USA, Expanded Abstracts, 3083–3086.

Jiao J., Stoffa P.L., Sen M.K. and Seifoullaev R.K. 2002. Residual migration-velocity analysis in the plane-wave domain. *Geophysics* **67**, 1252–1269.

Lafond C.F. and Levander A.R. 1993. Migration moveout analysis and depth focusing. *Geophysics* **58**, 91–100.

Liu Z. and Bleistein N. 1995. Migration velocity analysis: Theory and an iterative algorithm. *Geophysics* **60**, 142–153.

MacKay S. and Abma R. 1992. Imaging and velocity estimation with depth-focusing analysis. *Geophysics* **57**, 1608–1622.

Mulder W.A. and ten Kroode A.P.E. 2002. Automatic velocity analysis by differential semblance optimization. *Geophysics* **67**, 1184–1191.

Nemeth T. 1995. Velocity estimation using tomographic depth-focusing analysis. 65th SEG meeting, Houston, Texas, USA, Expanded Abstracts, 465–468.

Paffenholz J., McLain B., Zaske J. and Keliher P. 2002. Subsalt multiple attenuation and imaging: Observations from the sigsbee 2b synthetic dataset. 72nd SEG meeting, Salt Lake City, Utah, USA, Expanded Abstracts, 2122–2125.

Rickett J. and Sava P. 2002. Offset and angle-domain common image-point gathers for shot-profile migration. *Geophysics* **67**, 883–889.

Sava P. 2003. Prestack residual migration in the frequency domain. *Geophysics* **67**, 634–640.

Sava P. and Biondi B. 2004a. Wave-equation migration velocity analysis – I: Theory. *Geophysical Prospecting* **52**, 593–606.

Sava P. and Biondi B. 2004b. Wave-equation migration velocity analysis – II: Subsalt imaging examples. *Geophysical Prospecting* **52**, 607–623.

Sava P., Biondi B. and Etgen J. 2005. Wave-equation migration velocity analysis by focusing diffractions and reflections. *Geophysics* **70**, U19–U27.

Sava P. and Fomel S. 2003. Angle-domain common image gathers by wavefield continuation methods. *Geophysics* **68**, 1065–1074.

Sava P. and Fomel S. 2006. Time-shift imaging condition in seismic migration. *Geophysics* **71**, S209–S217.

Sava P. and Vasconcelos I. 2011. Extended imaging condition for wave-equation migration. *Geophysical Prospecting* **59**, 35–55.

Sava P. and Vlad I. 2008. Numeric implementation of wave-equation migration velocity analysis operators. *Geophysics* **73**, VE145–VE159.

Shen P. and Calandra H. 2005. One-way waveform inversion within the framework of adjoint state differential migration. 75th SEG meeting, Houston, Texas, USA, Expanded Abstracts, 1709–1712.

Shen P., Stolk C. and Symes W. 2003. Automatic velocity analysis by differential semblance optimization. 73rd SEG meeting, Dallas, Texas, USA, Expanded Abstracts, 2132–2135.

Shen P. and Symes W.W. 2008. Automatic velocity analysis via shot profile migration. *Geophysics* **73**, VE49–VE59.

Soubaras R. and Gratacos B. 2007. Velocity model building by semblance maximization of modulated-shot gathers. *Geophysics* **72**, U67–U73.

Stolt R.H. 1996. Short note – A prestack residual time migration operator. *Geophysics* **61**, 605–607.

Stork C. 1992. Reflection tomography in the postmigrated domain. *Geophysics* **57**, 680–692.

Stork C. and Clayton R.W. 1991. An implementation of tomographic velocity analysis. *Geophysics* **56**, 483–495.

Symes W.W. 2008. Migration velocity analysis and waveform inversion. *Geophysical Prospecting* **56**, 765–790.

Symes W.W. and Carazzone J.J. 1991. Velocity inversion by differential semblance optimization. *Geophysics* **56**, 654–663.

Virieux J. and Operto S. 2009. An overview of full-waveform inversion in exploration geophysics. *Geophysics* **74**, WCC1–WCC26.

Wang B., Kim Y., Mason C. and Zeng X. 2008. Advances in velocity model-building technology for subsalt imaging. *Geophysics* **73**, VE173–VE181.

Wang B., Mason C., Guo M., Yoon K., Cai J., Ji J. and Li Z. 2009. Subsalt velocity update and composite imaging using reverse-time-migration based delayed-imaging-time scan. *Geophysics* **74**, WCA159–WCA166.

Wang B., Qin F., Dirks V., Guilaume P., Audebert F. and Epili D. 2005. 3D finite angle tomography based on focusing analysis. 78th SEG meeting, Las Vegas, Nevada, USA, Expanded Abstracts, 2546–2549.

Woodward M., Nichols D., Zdraveva O., Whitfield P. and Johns T. 2008. A decade of tomography. *Geophysics* **73**, VE5–VE11.

Woodward M.J. 1992. Wave-equation tomography. *Geophysics* **57**, 15–26.

Xie X.B. and Yang H. 2008. The finite-frequency sensitivity kernel for migration residual moveout and its applications in migration velocity analysis. *Geophysics* **73**, S241–S249.

Yang T. and Sava P. 2010. Moveout analysis of wave-equation extended images. *Geophysics* **75**, S151–S161.

Yilmaz O. and Chambers R.E. 1984. Migration velocity analysis by wave-field extrapolation. *Geophysics* **49**, 1664–1674.

## APPENDIX A: WAVE-EQUATION TOMOGRAPHIC OPERATOR

The construction of wave-equation tomographic operator **L** used in equation (11) starts from separating the total slowness $s$ into a known background $s_b$ and a slowness perturbation $\Delta s$, as shown in equation (9). Next, we linearize the depth wavenumber $k_z$ relative to the background slowness $s_b$ using a truncated Taylor expansion series expansion

$$k_z \approx k_{z_b} + \left.\frac{\partial k_z}{\partial s}\right|_{s_b} \Delta s(\mathbf{x}), \tag{A1}$$

where the depth wavenumber in the background medium is characterized by slowness $s_b(\mathbf{x})$ is

$$k_{z_b} = \sqrt{[\omega s_b(\mathbf{x})]^2 - |k_\mathbf{x}|^2}. \tag{A2}$$

Under the shot-record framework, wavefield reconstruction for the multi-offset experiment is performed by separate recursive extrapolation of the source and receiver wavefields, $u_s$ and $u_r$. Thus, source and receiver wavefield perturbations $\Delta u_s(\mathbf{x})$ and $\Delta u_r(\mathbf{x})$ caused at depth $z + \Delta z$ by slowness perturbation $\Delta s(\mathbf{x})$ at depth $z$ is obtained by subtraction of the wavefields extrapolated from $z$ to $z + \Delta z$ in the true and background models:

$$\begin{aligned}\Delta u_{s_{z+\Delta z}}(\mathbf{x}) &= e^{+ik_z\Delta z}u_{s_z}(\mathbf{x}) - e^{+ik_{z_b}\Delta Z}u_{s_z}(\mathbf{x}) \\ &= e^{+ik_{z_b}\Delta Z}\left[e^{+i\left.\frac{\partial k_z}{\partial s}\right|_{s_b}\Delta s(\mathbf{x})\Delta z} - 1\right]u_{s_z}(\mathbf{x}).\end{aligned} \tag{A3}$$

$$\begin{aligned}\Delta u_{r_{z+\Delta z}}(\mathbf{x}) &= e^{-ik_z\Delta z}u_{r_z}(\mathbf{x}) - e^{-ik_{z_b}\Delta Z}u_{r_z}(\mathbf{x}) \\ &= e^{-ik_{z_b}\Delta Z}\left[e^{-i\left.\frac{\partial k_z}{\partial s}\right|_{s_b}\Delta s(\mathbf{x})\Delta z} - 1\right]u_{r_z}(\mathbf{x}).\end{aligned} \tag{A4}$$

Here, $\Delta u_s(\mathbf{x})$ and $u_s(\mathbf{x})$ correspond to perturbed and background source wavefields at a given depth level $z$ and frequency $\omega$. $\Delta u_r(\mathbf{x})$ and $u_r(\mathbf{x})$ correspond to perturbed and background receiver wavefields at a given depth level $z$ and frequency $\omega$. A similar relation can be applied at all depths and all frequencies.

Equation (A3) and (A4) establish a non-linear relation between the wavefield perturbation $\Delta u(\mathbf{x})$ and slowness perturbation $\Delta s(\mathbf{x})$. Given the complexity and cost of numeric optimization based on non-linear relations between model and wavefield parameters, it is desirable to simplify this relation to a linear relation between model and data parameters. Assuming small slowness perturbations, i.e., small phase perturbations, the exponential function $e^{\pm i\left.\frac{\partial k_z}{\partial s}\right|_{s_b}\Delta s(\mathbf{x})\Delta z}$ can be linearized using the approximation $e^{i\phi} \approx 1 + i\phi$, which is valid for small values of the phase $\phi$. Thus, the wavefield perturbations for

both the source and receiver sides can be computed by the following equations:

$$\begin{aligned}\Delta u_s(\mathbf{x}) &\approx +i \left.\frac{\partial k_z}{\partial s}\right|_{s_b} \Delta z\, u_s(\mathbf{x})\Delta s(\mathbf{x}) \\ &\approx +i\Delta z \frac{\omega u_s(\mathbf{x})\Delta s(\mathbf{x})}{\sqrt{1-\left[\frac{|k_x|}{\omega s_b(\mathbf{x})}\right]^2}},\end{aligned} \tag{A5}$$

and

$$\begin{aligned}\Delta u_s(\mathbf{x}) &\approx -i \left.\frac{\partial k_z}{\partial s}\right|_{s_b} \Delta z\, u_r(\mathbf{x})\Delta s(\mathbf{x}) \\ &\approx -i\Delta z \frac{\omega u_r(\mathbf{x})\Delta s(\mathbf{x})}{\sqrt{1-\left[\frac{|k_x|}{\omega s_b(\mathbf{x})}\right]^2}}.\end{aligned} \tag{A6}$$

The image perturbation at depth $z$ is obtained from the source and receiver scattered wavefields using the relation

$$\Delta r(\mathbf{x}) = \sum_{\omega} \left( \overline{u_s(\mathbf{x},\omega)}\Delta u_r(\mathbf{x},\omega) + \overline{\Delta u_s(\mathbf{x},\omega)} u_r(\mathbf{x},\omega) \right), \tag{A7}$$

which corresponds to the frequency-domain zero-lag cross-correlation of the source and receiver wavefields.

The tomographic operator $\mathbf{L}$ involves computing the wavefield perturbations using equations (A5) and (A6) and the image perturbation using equation (A7). Therefore, given a slowness perturbation $\Delta s$, the relating image perturbation is constructed via the operator $\mathbf{L}$. A more detailed implementation of operator $\mathbf{L}$ and its adjoint can be found in Sava and Vlad (2008).